Noname manuscript No.
(will be inserted by the editor)

Forced Changes to 20th Century ENSO Diversity in a Last Millennium Context

Samantha Stevenson · Antonietta Capotondi · John Fasullo · Bette Otto-Bliesner

Received: date / Accepted: date

Abstract The El Niño/Southern Oscillation (ENSO) exhibits considerable differences between the evolution of individual El Niño and La Niña events ('ENSO diversity'), with significant implications for impacts studies. However, the degree to which external forcing may affect ENSO diversity is not well understood, due to both internal variability and potentially compensatory contributions from multiple forcings. The Community Earth System Model Last Millennium Ensemble (CESM LME) provides an ideal testbed for studying the sensitivity of 20th century ENSO to forced climate changes, as it contains many realizations of the 850-2005 period with differing combinations of forcings. Metrics of ENSO amplitude and diversity are compared across LME simulations, and although forced changes to ENSO amplitude are generally small, forced changes to diversity are often detectable. Anthropogenic changes to greenhouse gas and ozone/aerosol emissions modify the persistence of Eastern and Central Pacific El Niño events, through shifts in the upwelling and zonal advective feedbacks; these influences generally cancel one another over the 20th century. Other forcings can also be quite important: land use changes amplify Eastern Pacific El Niño events via modulating zonal advective heating, and orbital forcing tends to preferentially terminate 20th century Central Pacific El Niño events due to enhanced eastern Pacific cooling during boreal winter and spring. Our results indicate that multiple anthropogenic and natural forcings can have substantial impacts on ENSO diversity, and suggest that correctly representing the net ENSO diversity response to climate change will depend on the precise balance between all these influences.

Keywords El Niño/Southern Oscillation · Climate variability · Climate modeling · Tropical Pacific · Climate dynamics

1 Introduction

The El Niño/Southern Oscillation (ENSO) dominates climate variability on interannual timescales, leading to drastic changes in sea surface temperature patterns which influence extreme weather events around the world (Ropelewski and Halpert, 1987). As such, it is vital to understand how projected future warming will impact ENSO. To date, multi-model studies have not been able to converge on a consensus regarding future ENSO

S. Stevenson · J. Fasullo · B. L. Otto-Bliesner
Climate & Global Dynamics Division, National Center for Atmospheric Research, 1850 Table Mesa Dr. Boulder, CO USA
Tel.: +1-303-497-1773
E-mail: samantha@ucar.edu

A. Capotondi
Physical Sciences Division, National Oceanic & Atmospheric Administration, Boulder, CO USA

projections (Collins et al., 2010; Stevenson, 2012; Bellenger et al., 2014) for reasons which remain unclear: one possible explanation is ENSO's sensitivity to small changes in atmosphere/ocean feedbacks (Philip and van Oldenborgh, 2006) which show differing responses to CO_2 increases. The large extent of unforced ENSO variability, however, also contributes to differences among centennial-scale climate projections (Stevenson et al., 2012b; Stevenson, 2012).

In addition to examining ENSO amplitude responses, understanding how the characteristics of El Niño and La Niña events are affected by climate change can provide important insights. Multiple 'flavors' of El Niño events have been documented over the instrumental period (Ashok et al., 2007): these so-called 'Eastern' and 'Central' Pacific El Niño varieties are thought to result from changes to the relative importance of various atmosphere/ocean feedbacks (see review by Capotondi et al. (2015)). The development of each El Niño event is unique (Kessler, 2002), but modeling studies suggest the possibility for alteration of the dominant ENSO varieties by changes to the mean climate (Yeh et al., 2009). This has implications for the overall degree of ENSO variability expected in the future, as well as for the remote impacts expected from varying types of ENSO (Yu et al., 2012).

The response of ENSO diversity to external forcing is still an open question, and one which depends on the balance between all relevant forcing factors. To date there has been very little work on the subject: although some paleoclimate studies suggest a role for ENSO diversity shifts during the mid-Holocene forced by orbital changes (Karamperidou et al., 2015), more recent periods have not been thoroughly investigated. Even over the 20th century, influences from land use changes and anthropogenic aerosol emissions are known to have impacted the climate (Pielke et al., 2002; Kalnay and Cai, 2003), in addition to greenhouse gas increases. As all of these factors affect the mean climate of the tropics (Collins et al., 2010), their net effect may alter ENSO diversity as well. Identifying these influences, however, requires ensembles of simulations containing sufficiently long time series to average over internal variability - something which has not been possible in previous modeling investigations.

The development of the NCAR Community Earth System Model Last Millennium Ensemble (CESM LME; Otto-Bliesner et al. (2016)) provides a modeling testbed uniquely suited to diagnosing ENSO diversity responses to climate change. The LME simulates influences from anthropogenic (greenhouse gas emissions, ozone and tropospheric aerosols, and land use/land cover changes) and natural (orbital changes, solar irradiance, and volcanic eruptions), both simultaneously and individually. All ensembles extend from 850-2005AD, much longer than the timescale of internal ENSO variability (Stevenson et al., 2010, 2012b,a).

The manuscript is organized into several sections: the LME and overall millennial climate trends are discussed in Section 2, and 20th century changes to the mean climate and the seasonal cycle are described in Section 3. M etrics used to diagnose ENSO diversity are presented in Section 4, and a mixed-layer heat budget analysis is used in Section 5 to identify the mechanisms for ENSO diversity responses. Implications and conclusions are discussed in Section 6.

2 The Last Millennium Ensemble

All of the simulations currently included in the LME are analyzed here; additional ensemble members have been added since the initial publication of the ensemble (Otto-Bliesner et al., 2016), and the simulations included in this analysis are summarized in Table 1. All simulations are run at an atmosphere/land resolution of 2°, while a variable-resolution ocean grid is used, ranging from 1° in the midlatitudes to 0.3° near the equator. For analysis purposes, the data output from the LME are split into 'pre-industrial' (850-1849) and '20th century' (1850-2005) components. We note that this separation does lead to significant differences in the length of the two comparison segments, and for the 20th century case some contribution from unforced centennial ENSO variability may be present (*c.f.* Wittenberg (2009); Stevenson et al. (2010)); however, in order to isolate anthropogenic influences this choice is unavoidable.

The details of the forcing factors applied are discussed in Otto-Bliesner et al. (2016): greenhouse gas concentrations (CO_2, CH_4, and N_2O) are derived from Antarctic ice core reconstructions which cover the entire past millennium (Schmidt et al., 2011). No ozone or tropospheric aerosol reconstruction data was available prior to

1850, and therefore the 850 control simulation is used as the 'pre-industrial' component of the ozone/aerosol (hereafter O3AER) ensemble. After 1850, ozone concentrations are specified based on output from simulations with a high-top chemistry/climate model (the Whole Atmosphere Community Climate Model; Marsh et al. (2013)) using specified concentrations of ozone-depleting substances. Post-1850 anthropogenic aerosol emissions were prescribed based on historical estimates created for use in the Coupled Model Intercomparison Project version 5 (Lamarque et al., 2010), and concentrations allowed to vary prognostically based on the aerosol microphysical schemes in CAM5. These ozone and aerosol protocols are equivalent to those used in the CESM Large Ensemble, and are also discussed in Kay et al. (2015). Land use/land cover (LULC) changes are also simulated in the LME, following the Pongratz et al. (2009) reconstruction prior to 1500 and the Hurtt et al. (2011) reconstruction in subsequent years, with the two datasets merged at 1500; LULC forcing relates primarily to changes in the area covered by crop and pasture lands, as well as the extent of urbanization over 850-2005.

The natural forcings applied in the LME derive from volcanic eruptions, changes in solar irradiance, and orbital modulations. Changes to orbital eccentricity, obliquity, and precession lead to changes in latitudinally and seasonally dependent insolation, and are prescribed according to the formulation of Berger (1978). Changes in total solar irradiance (TSI) follow the Vieira et al. (2011) reconstruction combined with an imposed 11-year solar cycle which derives changes to spectral solar irradiance based on frequency-dependent regression on TSI (Schmidt et al., 2011). Volcanic influences are prescribed according to Gao et al. (2008), which uses sulfate deposits in Greenland and Antarctic ice cores combined with a simple, seasonally dependent aerosol transport model to derive zonal-mean loadings of stratospheric aerosols.

For large-scale context, the evolution in Northern Hemisphere surface air temperature is shown for all LME ensembles in Figure 1; over the pre-industrial period, volcanic eruptions provide the strongest control on climate, as indicated by the close correspondence between the 'full forcing' and 'volcanic' simulations. Long-term volcanically induced cooling leads to a lower overall NH temperature at 1850 in the full forcing ensemble relative to the other ensembles. Over the 20th century, the greenhouse gas and O3AER ensembles show opposing NH influences, with GHG-induced warming overcoming ozone/aerosol-induced cooling by the end of the century (roughly 1950-2005). Relatively little change is seen in the other ensembles (Figure 1b), with the exception of a slight cooling in the land use/land cover simulations.

The evolution of ENSO amplitude in the LME is shown in Figure 2, represented by the time series of 20-year running SST anomaly variance in the NINO3.4 region (5°S-5°N, 120-170°W). We also note that the O3AER case is represented only by the single 850 control simulation over the 850-1849 period. In all ensembles there is a large degree of decadal to centennial modulation of ENSO variability, consistent with previous millennial-scale GCM studies (Wittenberg, 2009; Stevenson et al., 2012a). There is a small tendency for shifts in the NINO3.4 variance as a result of 20th century climate forcing; this increase is near the threshold for detectability over 1850-2005, suggesting that 20th century climate change has not played a substantial role in altering ENSO amplitude relative to the last millennium, in contrast to paleoclimate reconstructions which show a 20th century ENSO strengthening (Cobb et al., 2013; McGregor et al., 2010). It should be noted, however, that projected ENSO amplitude increases do become significant in extensions of the full-forcing LME simulations during the 21st century (2005-2100), a result which is confirmed using future projections with the CESM Large Ensemble (Fasullo et al., 2016).

3 Changes to Mean and Seasonal Climatologies

Changes to ENSO diversity are generally interpreted in the context of changing the relevant feedback processes involved with the ENSO cycle, which are known to be connected with the mean climate (Fedorov and Philander, 2000; van Oldenborgh et al., 2005). Figure 3 shows composite differences in annual-mean SST and wind stress between the 20th century and pre-industrial period for the LME simulations. As expected, GHG emissions increase temperatures throughout the Pacific (Figure 3b); the warming is strongest in the eastern equatorial Pacific, and is accompanied by a reduction in the strength of the trade winds along the equator. This is consistent with

previous multi-model studies showing weakening of 21st century equatorial trades due to anthropogenic warming (Vecchi et al., 2006; Vecchi and Soden, 2007; Stevenson, 2012). In contrast, ozone/aerosol effects lead to cooling throughout the tropics and preferentially in the eastern equatorial region, accomparnied by strengthened trade winds (Figure 3c). These effects largely cancel over the eastern Pacific in the full forcing ensemble, but some GHG-driven warming does persist over the warm pool and the southeastern tropics (Figure 3a). Interestingly, there does not seem to be a coherent change in trade wind strength across the basin in the full forcing ensemble; westerly anomalies persist only roughly to the dateline. We also note that the warming of the southeastern tropics in these ensembles contrasts with previous studies of 21st century SST pattern formation (*i.e.* Xie et al. (2010)), in which the trades strengthen in this region and lead to reduced warming.

In the remaining LME ensembles (Figure 3d-g), changes to 20th century mean circulation are much smaller. The land use/land cover ensemble (Figure 3d) shows a slight cooling and easterly wind anomalies in the western Pacific, and an antisymmetric wind stress pattern in the eastern Pacific subtropics with northeasterly (northwesterly) anomalies in the Northern and Southern Hemispheres, respectively. The causes for this pattern are left for future investigation, but likely relate to cooling of the North American continent (not pictured). Volcanic forcing also creates 20th century changes, preferentially cooling the eastern Pacific and strengthening the equatorial trades (Figure 3g). Minimal SST changes are apparent in the solar and orbital ensembles (Figure 3e,f).

Changes to the vertical structure of the ocean are also apparent as a result of 20th century climate change. Figure 4 shows the difference in annual-mean temperature averaged over 2°S-2°N, between the 20th c. and pre-industrial periods for the LME simulations. The GHG ensemble clearly demonstrates an increase in vertical stratification, with surface-intensified warming particularly apparent in the eastern equatorial Pacific (Figure 4b). In constrast, the O3AER ensemble shows an overall cooling intensified at the surface, which creates a net decrease in thermal stratification (Figure 4c). The full-forcing ensemble once again shows a result tending to indicate the increased efficacy of GHG forcing (Figure 4a); warming at the surface persists, particularly in the western equatorial Pacific. Vertical temperature changes in all other ensembles are significantly smaller (Figure 4d-g), indicating that stratification changes are less likely to play a role in modulating ENSO diversity in these ensembles (see also Section 5). We note that the temperature changes near 150-200m in both the GHG and O3AER ensembles tend to oppose the tendencies at the surface (Figure 4b,c). This is a known feature of ocean circulation responses to forcing in coupled climate models, and relates to changes in the subtropical cell; under greenhouse-induced heating, the subtropical cell has been shown to slow as a result of the decrease in wind stress curl in previous versions of the CESM (Stevenson et al., 2012a), leading to reduced transport of warm water to this location. As the patterns of wind stress change in the O3AER ensemble tend to oppose the GHG-induced anomalies, we expect that the heating near 200m in this ensemble is a result of a corresponding increase in subtropical cell circulation.

20th century changes to the seasonal cycle of the equatorial Pacific (2°S-2°N) are shown for each ensemble in Figure 5. The pre-industrial climatologies are similar across ensembles, with eastern Pacific SST at its minimum in October. However, changes to seasonality across ensembles differ dramatically: as was the case for mean SST (Figure 3), greenhouse gas and ozone/aerosol emissions lead to the strongest signals and come close to canceling one another. In both cases, the largest temperature difference occurs in boreal spring: cooling from ozone/aerosol emissions appears to dominate over GHG warming in the eastern Pacific in the full forcing ensemble (Figure 5b). In the other ensembles, the strongest changes to seasonality are observed in the orbital and solar forcing cases, both of which show an overall increase in zonal SST gradient (Figure 5j,l) which is enhanced during boreal spring (solar) and fall (orbital).

4 Changes to ENSO Diversity

We next examine changes to ENSO behavior through metrics of ENSO diversity. The identification of El Niño events as 'Eastern' or 'Central' may be done by many different methods; to ensure robustness, we have applied multiple metrics, following several definitions:

- The index-based method of Yeh et al. (2009): El Niño events are identified as periods in which the Oceanic NINO Index (ONI) value is above 1σ, where the ONI is defined as the 3-month running SST anomaly over the NINO3.4 region (5°S-5°N, 120°-170°W), relative to a moving 30-year climatology. Events with ONI above 1σ are then classified into Eastern or Central types according to whether the temperature is larger in NINO3 (5°S-5°N, 90-150°W) or NINO4 (5°S-5°N, 160°E-150°W).
- The definition of Kug et al. (2010), which is similar to the Yeh et al. (2009) version but defines Eastern and Central Pacific El Niño events simply on the basis of having NINO3 and NINO4 DJF SSTA above 1σ, respectively. Here we have applied a bias correction to this definition following Capotondi (2013), in which the region boxes used are shifted west by 20° to compensate for structural biases in the mean fields of SST simulated by climate models.
- The EOF-based definition of Kao and Yu (2009), in which the Eastern and Central Pacific El Niño structures are identified by taking the leading EOF mode after removal by linear regression of influences from other regions: to isolate Eastern Pacific El Niño, NINO4 is regressed out to emphasize Eastern Pacific variability, and to isolate Central Pacific El Niño, NINO1+2 (0-10°S, 90-80°W) is removed. For consistency the EP and CP modes are calculated through EOF analysis using the LME 850 control. These modes were then used for all simulations. The corresponding EP and CP indices were computed by projecting the SST fields for each simulation on the EP and CP patterns. All El Niño events were first identified by requiring that the ONI index exceed 1σ during DJF, and classified into EP or CP based on the relative values of the EP and CP indices during DJF.

Figure 6 shows the relative proportions of EP and CP El Niño events identified using all of the above metrics, for the pre-industrial and 20th century portions of the LME ensembles. In all cases, the CP El Niño events are much less frequent than the EP, in contrast to previous versions of the CESM (Stevenson et al., 2012a) and in relatively good agreement with 20th century observations (Yeh et al., 2009). Changes to event proportions between the 20th century and pre-industrial are fairly small in all ensembles - in the full forcing case, no significant changes are observable using any metric, and the same is true for volcanic and solar forcing ensembles. In some ensembles, there are detectable changes to event proportions, but the magnitude of pre-industrial/20th century differences are strongly metric-dependent. Land use/land cover changes and greenhouse gas increases both lead to increases in CP El Niño fraction by a single metric: for land use/land cover, Kao and Yu (2009) and for greenhouse gases, Yeh et al. (2009). The only two ensembles which show changes in event fraction consistently across multiple metrics are the orbital and O3AER, which both tend to enhance the CP:EP El Niño ratio according to the Kao and Yu (2009) and Yeh et al. (2009) metrics. In the O3AER ensemble, the increased equatorial trade winds are associated with a stronger zonal thermocline gradient (not pictured). Thus the enhanced 20th century CP El Niño frequency is consistent with previous work showing a link between thermocline gradient and CP proportion (McPhaden et al., 2011; Capotondi and Sardeshmukh, 2015). The orbital influence is not associated with a strong mean-state change, but may relate to the enhanced Eastern Pacific cooling during boreal fall (Figure 5j) which preferentially terminates CP El Niño and could potentially allow these events to recur more frequently.

Although the results in Figure 6 do depend on metric, for a more detailed examination of the mechanisms for ENSO flavor shifts it is necessary to choose a single definition. Here we adopt the Kao and Yu (2009) metric, as it incorporates a more physically meaningful definition of El Niño *via* the use of EOF modes from the LME 850 control. Composite evolution patterns for equatorial Pacific SSTA during EP and CP El Niño years are shown in Figures 7 and 8 for each ensemble; composites are calculated for a period +/- 24 months relative to the January corresponding to the DJF period in which the event peaks (hereafter 'Year 0'). Here both the differences between the pre-industrial portions of the forced ensembles with the 850 control (Figure 7, 8 left-hand panels) and the difference between the 20th century and pre-industrial portions of each ensemble (Figure 7, 8 right-hand panels) are shown. EP El Niño evolution is not significantly altered in the full forcing 20th century ensemble (Figure 7b,c) but examining the remaining panels shows that this lack of response results from compensation between multiple, fairly strong, influences from individual forcings. Greenhouse gas increases enhance the termination of EP El Niño events and strengthen the La Niña events which follow (Figure 7e). In contrast, the O3AER ensemble

shows more persistent 20th century EP El Niño events and weaker subsequent La Niña development (Figure 7g), although changes become significant only in the western Pacific roughly 12 months following the event peak. The strongest influence on the peak phase of EP El Niño events is actually land use/land cover changes (Figure 7h,i), which strongly enhance SST anomalies in the eastern Pacific. Orbital, solar, and volcanic forcings have much weaker influences on EP El Niño; although slight reductions in peak SSTA appear in the solar and volcanic ensembles, this cooling is largely insignificant.

Forced changes to CP events are quite distinct from the CP patterns (Figure 8). Once again the greenhouse gas (Figure 8e) and O3AER (Figure 8g) ensembles show SST anomalies which oppose one another; in this case, GHG increases lead to more persistent CP El Niño and ozone/aerosol emissions enhance CP El Niño termination while reducing the peak strength of the event. However, for CP El Niño events the strongest control appears to be orbital forcing (Figure 8j,k): strong negative eastern Pacific SST anomalies are created by 20th century orbital changes, preferentially terminating CP El Niño events. When all forcings are included, the combined influence of orbital forcing and ozone/aerosol emissions seems to outweigh the GHG impact on CP El Niño events, as evidenced by the negative SSTA at 10 months post-event peak in the full forcing ensemble (Figure 8c).

5 Mixed-Layer Heat Budget

To examine the mechanisms for changes to El Niño properties in the LME simulations, we have performed a mixed-layer heat budget analysis over the equatorial Pacific. The formulation of this heat budget follows Graham et al. (2014):

$$\frac{\partial T'}{\partial t} = Q' - \bar{u}\cdot\nabla T' - u'\cdot\nabla\bar{T} - u'\cdot\nabla T' + \overline{u'\cdot\nabla T'} - w'\frac{(\overline{T_{MLD}} - \overline{T_{sub}})}{H} - \bar{w}\frac{T'_{MLD} - T'_{sub}}{H} - w'\frac{(T'_{MLD} - T'_{sub})}{H} \quad (1)$$

where T_{MLD} indicates the temperature within the mixed layer, T_{sub} the temperature immediately below the mixed layer, Q the net surface shortwave heat flux, and overbars indicate 12-month climatologies in the relevant variable and primes the deviations from those climatologies. The mixed-layer depth H used here is that of Large et al. (1997), who define the mixed layer as the shallowest layer where the local, interpolated buoyancy gradient is equal to the maximum gradient between the surface and any arbitrary depth within the water column. We note that the mixed layer depth is specified as a fully spatially and temporally variable field, rather than a fixed depth value as has been applied in previous studies (Kug et al., 2010; Di Nezio et al., 2012; Capotondi, 2013). We find that this is the most physically accurate method of specifying mixed-layer depth, but does lead to a significant increase in the magnitude of the upwelling feedback ($w'\frac{\partial\bar{T}}{\partial z}$) relative to the thermocline feedback ($\bar{w}\frac{\partial T'}{\partial z}$) found to dominate in those studies. Part of the reason for this difference is that the Large et al. (1997) definition tends to give relatively deep MLD values, which damps the thermocline feedback term.

Here entrainment into the mixed layer is represented using the entrainment velocity

$$w = \frac{\partial H}{\partial t} + \mathbf{u}\cdot\nabla H + w_H \quad (2)$$

where w_H is the vertical velocity immediately below the mixed layer. The degree of shortwave flux penetrating the mixed layer is calculated following Pacanowski and Griffies (1999); Huang et al. (2010):

$$Q_{pen} = Q_{sw}(0.58e^{\frac{-H}{0.35}} + 0.42e^{\frac{-H}{23}}) \quad (3)$$

Results from the heat budget analysis are shown in Figures 9 and 10; here the major budget terms are composited over all EP and CP El Niño events, for the period 24 months prior to 24 months after the January of the DJF in which the event peaks ('Year -2' to 'Year +1'). We follow the conventions adopted by Capotondi (2013), averaging budget terms over 2.5°S-2.5°N, 190-250°E ('NINO3m') and 2.5°S-2.5°N, 140-190°E ('NINO4m') for EP and CP El Niño events, respectively. We also apply an 18 month - 7 year bandpass filter to the time series of all

budget terms prior to compositing, in order to isolate the interannual variability; the results are not dramatically sensitive to the application of the filter. Space limitations do not allow display of all budget terms, but generally speaking the dominant balance for EP El Niño events is between the upwelling, zonal advective ($u' \frac{\partial \bar{T}}{\partial x}$), and surface heat flux feedbacks for both types of event. The upwelling feedback is stronger during EP events (Figure 9) than CP (Figure 10), but in both cases the zonal advective feedback tends to create more heating than the upwelling feedback. We also note that the surface flux feedback term does change in response to forcing (not pictured), which appears to relate primarily to shifts in the net heat flux damping in response to changes in the magnitude of SST anomalies. Thus, we believe that the surface flux term reflects a response to changes in other terms in the heat budget, rather than being a causal factor in ENSO evolution.

Comparison of the colored envelopes in Figures 9 and 10 illustrates the changes taking place as a result of external forcing. Under greenhouse forcing, the upwelling feedback after the peak of El Niño (a negative value) becomes more negative in the 20th century relative to the pre-industrial (Figure 9c). This occurs at the time in the ENSO cycle (5-10 months after El Niño peak) when Figure 7d showed an enhanced tendency for El Niño termination, indicating that the enhanced vertical stratification (Figure 4b) is creating more efficient cooling when upwelling resumes following peak El Niño. In the ozone/aerosol ensemble, the opposite response is seen in the upwelling feedback term (Figure 9e); the lower vertical stratification (Figure 4c) leads to less efficient El Niño termination in the 20th century due to aerosol impacts.

Figure 9h also reveals that the land use/land cover-induced amplification of 20th century EP El Niño events is caused by an enhanced zonal advective feedback prior to the event peak. The changes to the mean SST gradient due to land use are small (Figure 9d); the strengthened zonal advective feedback relates to enhanced zonal current anomalies during El Niño development (not pictured). The causes for the enhanced current anomalies are not clear, but may relate to preferential western Pacific cooling during boreal summer (Figure 5h) and the associated reduction in trade wind strength; weaker overall trade winds are expected to allow more efficient excitation of anomalous currents through wind stress anomalies.

Changes to CP El Niño evolution under 20th century forcing, although smaller than their EP counterparts, can also be explained through changes to the upwelling and zonal advective feedbacks. The strongest response is seen in the orbital ensemble, in which the zonal advective feedback is much more strongly negative 6-10 months following the event peak during the 20th century (Figure 10j) as a result of orbitally induced cooling in the Eastern Pacific during boreal fall (Figure 5j). Greenhouse gas forcing leads to the zonal advective feedback remaining positive for longer following El Niño peak (Figure 10d), which causes the observed slight enhancement in CP event persistence in Figure 10d (although the significance of both changes is quite low). Ozone/aerosol forcing has the opposite effect, leading to negative anomalies in both the zonal advective and upwelling feedbacks post-event peak (Figure 10e,f). As the zonal SST gradient is reduced under 20th century forcing in the GHG ensemble and is increased in the O3AER ensemble, one would expect that this should lead to weakening of the zonal advective term in the GHG and strengthening in O3AER, respectively - the opposite of what is observed in Figure 10e,f. Anomalous currents are again responsible for the zonal advective feedback responses, and we hypothesize that stronger equatorial trades in the O3AER ensemble suppress the ability of wind anomalies to excite these anomalous currents.

6 Conclusions

This study has analyzed simulations performed as part of the CESM Last Millennium Ensemble to identify the relative contributions of natural and anthropogenic forcing to 20th century changes to ENSO diversity. The major controls on mean climate are greenhouse gas-driven warming and tropospheric ozone/aerosol-driven cooling during the 20th century, and volcanic eruptions during the pre-industrial period, with some contribution from solar irradiance and land use changes. However, although mean temperature varies considerably, no strong trends in ENSO amplitude are apparent in the 20th century relative to the last millennium. This may indicate

Table 1 Simulations in the Last Millennium Ensemble analyzed for the present study.

Ensemble Name	# Simulations
Full forcing	13
Greenhouse gas only	3
Ozone/aerosol only	5
Land use/land cover only	3
Solar only	4
Orbital only	3
Volcanic only	5

either an underestimate of reconstructed ENSO variance trends (Cobb et al., 2013; McGregor et al., 2010) or the importance of internal variability in the ENSO system.

Forced changes to ENSO diversity are apparent in the LME, despite the lack of ENSO amplitude response. Changes are generally apparent only in the single-forcing ensembles, as the combined influence of forcing factors tends to cancel the majority of the signal in the full-forcing ensemble. The relative proportion of CP and EP El Niño events increases due to both anthropogenic ozone/aerosol emissions and orbital forcing changes; all other forcings show either a null response or one which is inconsistent in sign across definitions of CP vs. EP events. Notably, greenhouse gas increases do not appear to favor the development of CP El Niño events, in contrast with previous studies (Yeh et al., 2009).

The evolution patterns of EP and CP El Niño events respond to 20th century forcings, although again exhibiting a tendency to cancel one another in the full forcing ensemble. EP El Niño events are preferentially terminated under GHG increases, due to more efficient upwelling-induced cooling in a more strongly stratified equatorial eastern Pacific. The reverse is true for ozone/aerosol forcing, as stratification reductions inhibit EP El Niño termination via the upwelling feedback. Land use/land cover changes also strongly amplify EP El Niño events. This takes place by enhancing the zonal advective feedback during El Niño development, a result of stronger westerly current anomalies.

Central Pacific El Niño events also exhibit compensating influences from GHG and O3AER forcing, but are most strongly affected by orbital changes. GHG increases lead to a slight and marginally significant enhancement in the post-El Niño peak zonal advective feedback, while ozone/aerosol forcing has the opposite effect. This appears related to enhanced zonal current anomalies in regimes of reduced zonal SST gradient, although the mechanism for this relationship is still unclear. Orbital forcing alters the seasonal cycle of equatorial SST, preferentially cooling the eastern Pacific during boreal winter and spring; this enhances the zonal SST gradient during El Niño termination and leads to a much more strongly negative zonal advective feedback at that time. Both this and the EP El Niño results highlight the potential for natural forcing to affect ENSO diversity, even in strongly anthropogenically perturbed climates.

These results cannot be generalized without replication using additional climate models, but suggest the potential importance of multiple forcing factors to ENSO diversity projections under climate change. For instance, the treatment of aerosols varies widely from model to model, both in terms of the physical properties of emitted particles and in the simulation of aerosol evolution. Many climate change projections also use a fixed, pre-industrial orbital configuration, and the implementation of land use/land cover changes is well known to differ dramatically across models. Our results indicate that these effect may have strong implications for ENSO diversity responses, and for the ability of current multi-model experiments to properly isolate the mechanisms for those responses. It is not clear whether the cancellation between forcings in the LME is a behavior unique to CESM - if not, small differences in modeled sensitivites to different forcings might be expected to lead to large changes in ENSO diversity projections. We recommend further investigation into the contribution of individual natural and anthropogenic forcings to future projections of ENSO characteristics.

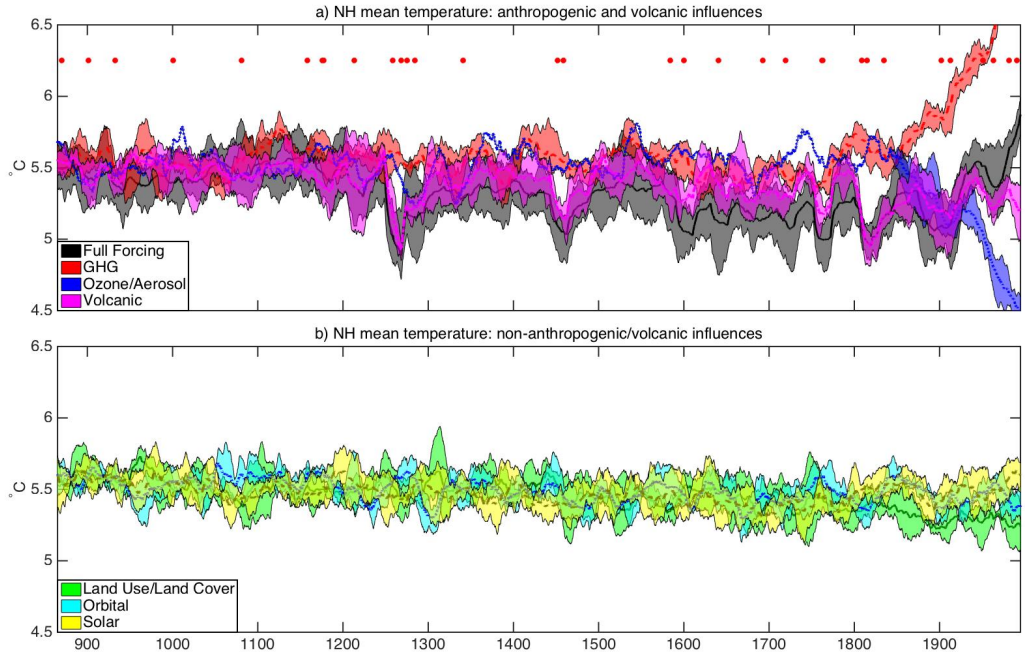

Fig. 1 Northern Hemisphere mean temperature time series for LME ensembles forced by a) greenhouse gas, ozone/aerosol, and volcanic influences, as well as all forcings combined; and b) land use/land cover, orbital changes, and solar irradiance. Filled red circles in panel a) indicate the occurrence years for major volcanic eruptions over 850-2005.

Acknowledgements This work is supported by an NSF EaSM grant (AGS 1243125). The CESM project is supported by the National Science Foundation and the Office of Science (Biological and Environmental Research program) of the U.S. Department of Energy. Computing resources were provided by the Climate Simulation Laboratory at NCARs Computational and Information Systems Laboratory (CISL), which is sponsored by the National Science Foundation and other agencies.

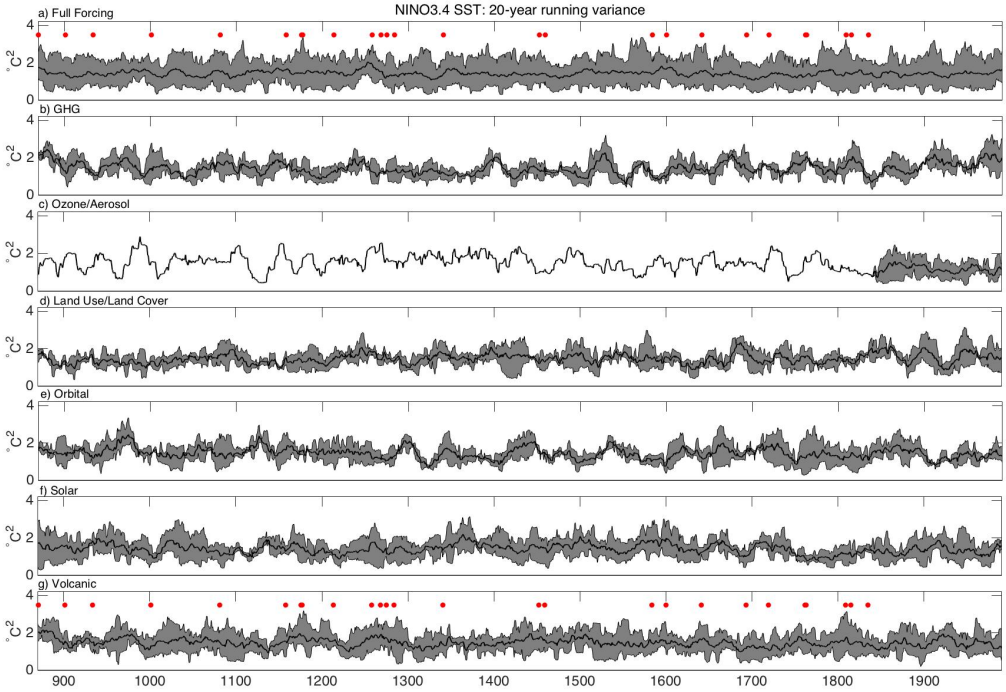

Fig. 2 20-year running variance in NINO3.4 SSTA in the LME ensembles. a) Full forcing, b) greenhouse gas only, c) ozone and anthropogenic aerosol only, d) land use/land cover only, e) orbital only, f) solar only, and g) volcanic only. As in Figure 1, filled red circles indicate major volcanic eruptions.

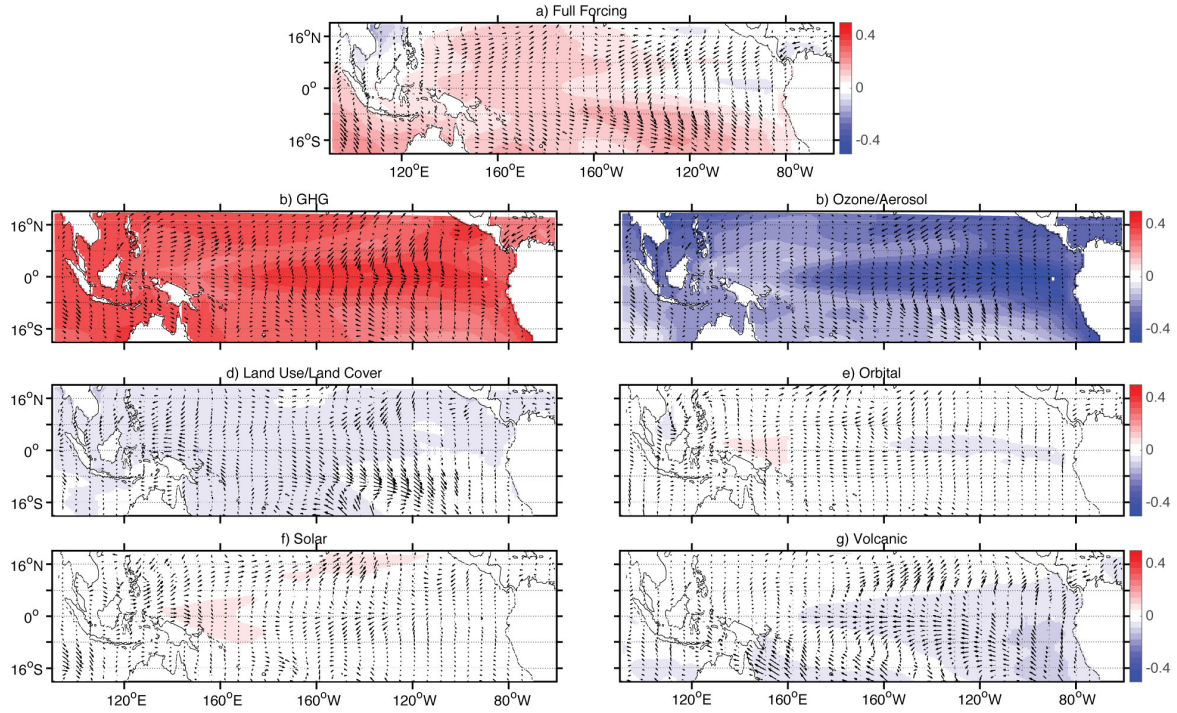

Fig. 3 Differences in annual-mean SST (°C; colors) and wind stress (m/s; arrows) between the 20th century and pre-industrial period, for the LME a) full forcing, b) GHG-only, c) ozone/aerosol only, d) land use/land cover only, e) orbital only, f) solar only, and g) volcanic only ensembles.

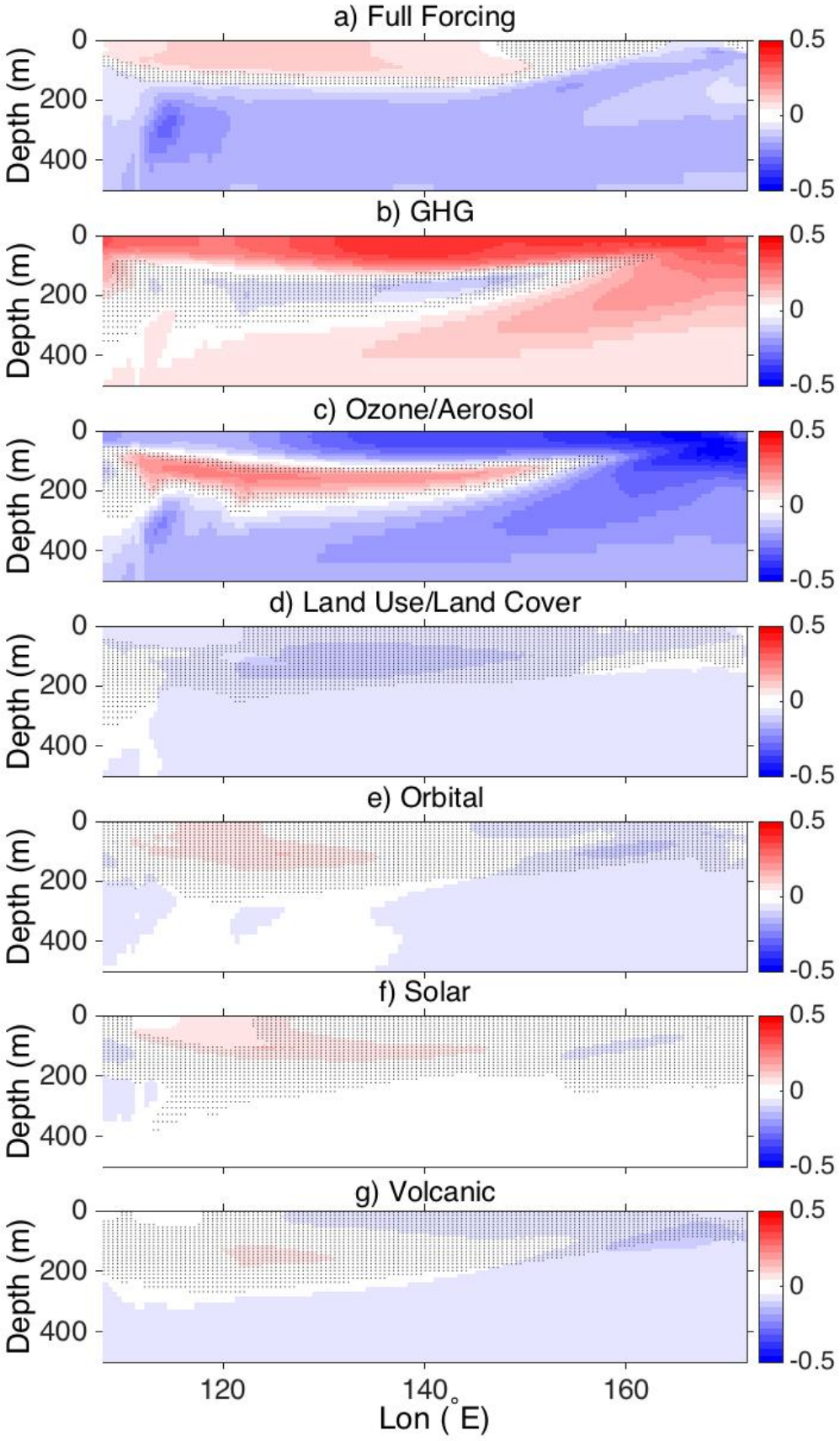

Fig. 4 Differences in equatorially averaged annual temperature (°C) between the 20th century and pre-industrial period, for the LME a) full forcing, b) GHG-only, c) ozone/aerosol only, d) land use/land cover, e) orbital, f) solar, and g) volcanically forced ensembles. Stippling indicates differences between the 20th century and pre-industrial insignificant at 90% using a Wilcoxon rank-sum test.

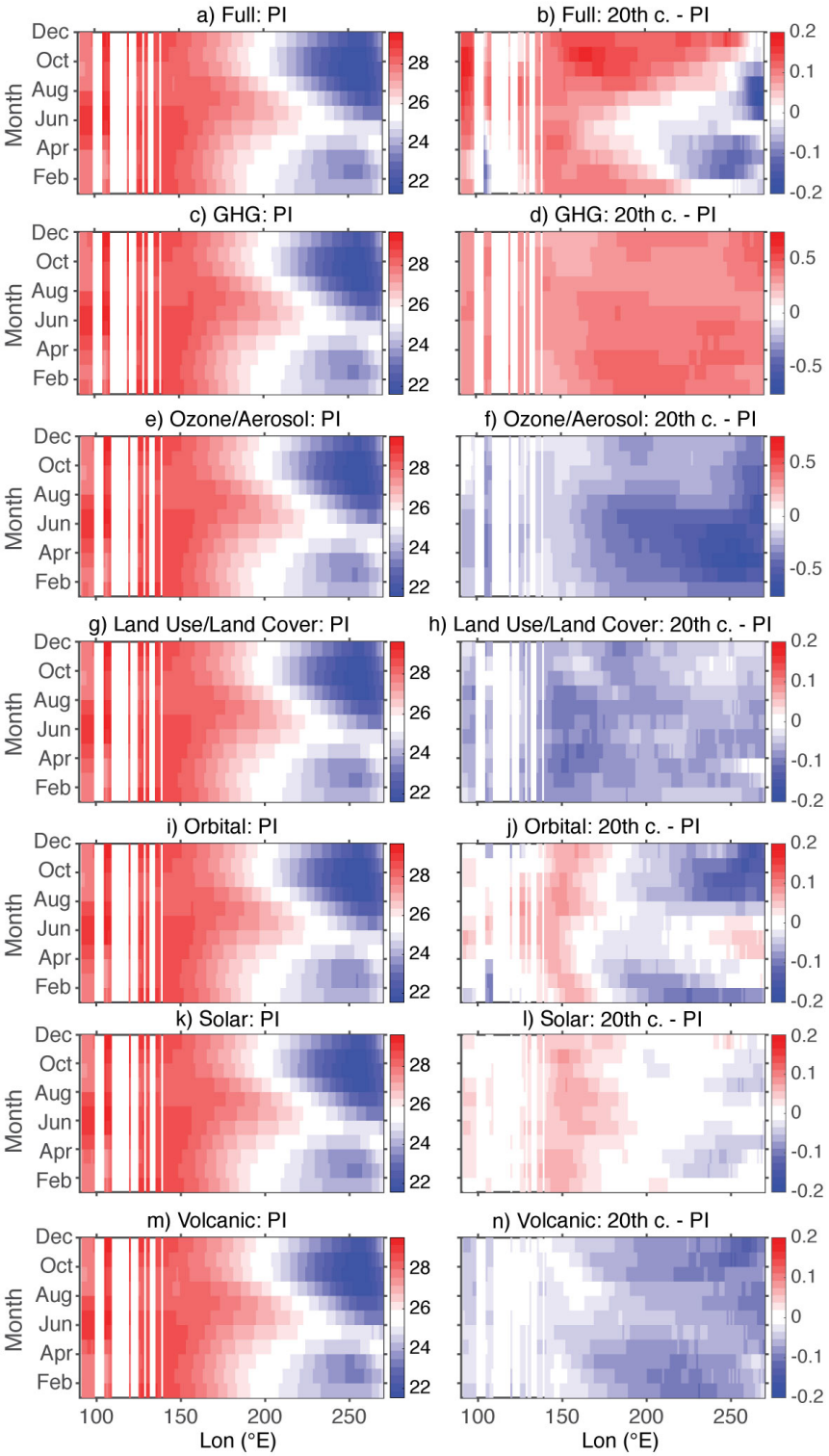

Fig. 5 Composite equatorial (2°S-2°N) sea surface temperature versus calendar month over the pre-industrial period (left column) and the difference between the 20th century and pre-industrial (right column), for the LME a)-b) full forcing, c)-d) GHG-only, e)-f) ozone/aerosol only, g)-h) land use/land cover, i)-j) orbital, k)-l) solar, and m)-n) volcanically forced ensembles.

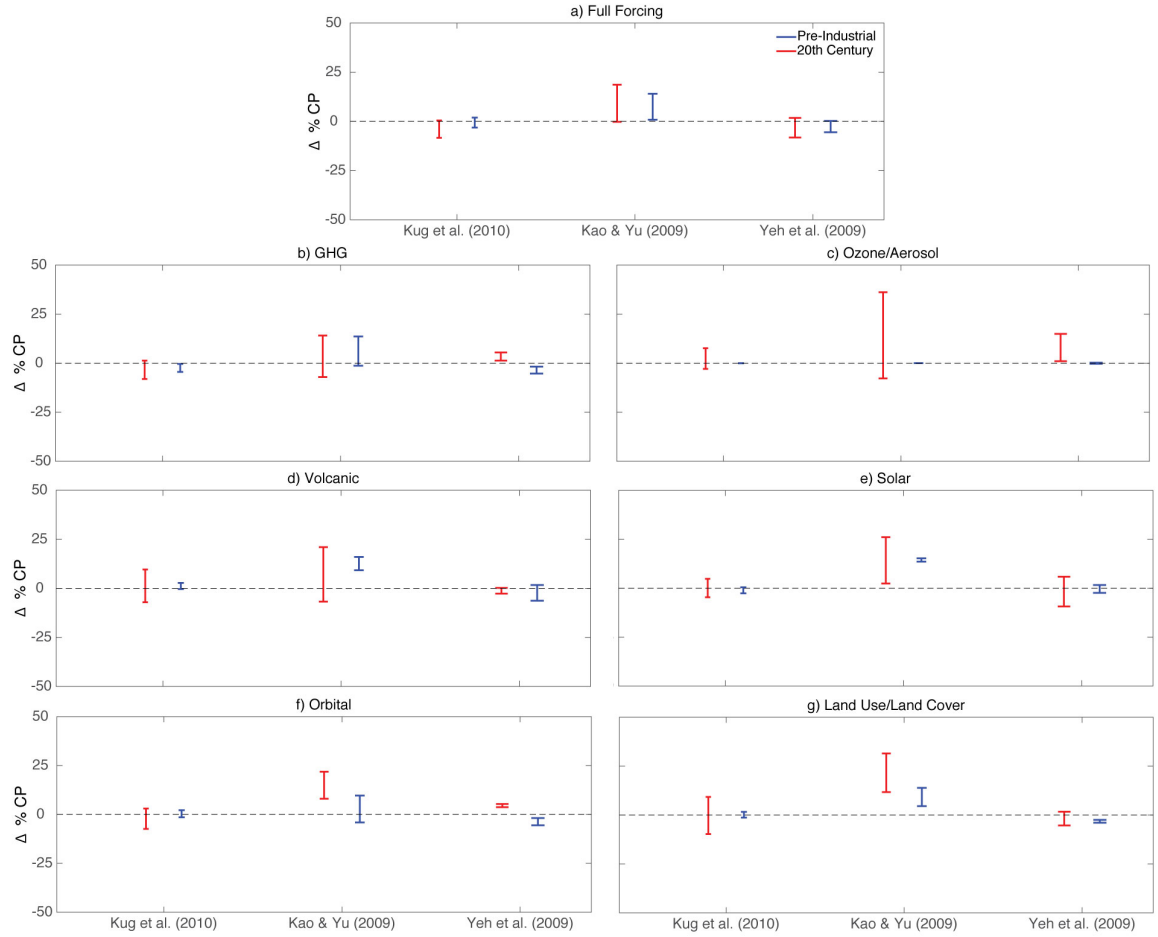

Fig. 6 Proportion of CP El Niño events in the LME ensembles during the pre-industrial period (850-1849; blue) and the 20th century (1850-2005; red), using the ENSO diversity metrics described in the main text: the index-based methods of Kug et al. (2010) and Yeh et al. (2009), and the EOF-based method of Kao and Yu (2009). Bars indicate the interquartile range associated with CP El Niño occurrence frequency for each metric, and all frequencies are expressed as differences relative to the 850 control (CP occurrence fraction in the 850 control is 31% for the Kug et al. (2010) metric, 36% for Kao and Yu (2009), and 44% for Yeh et al. (2009)).

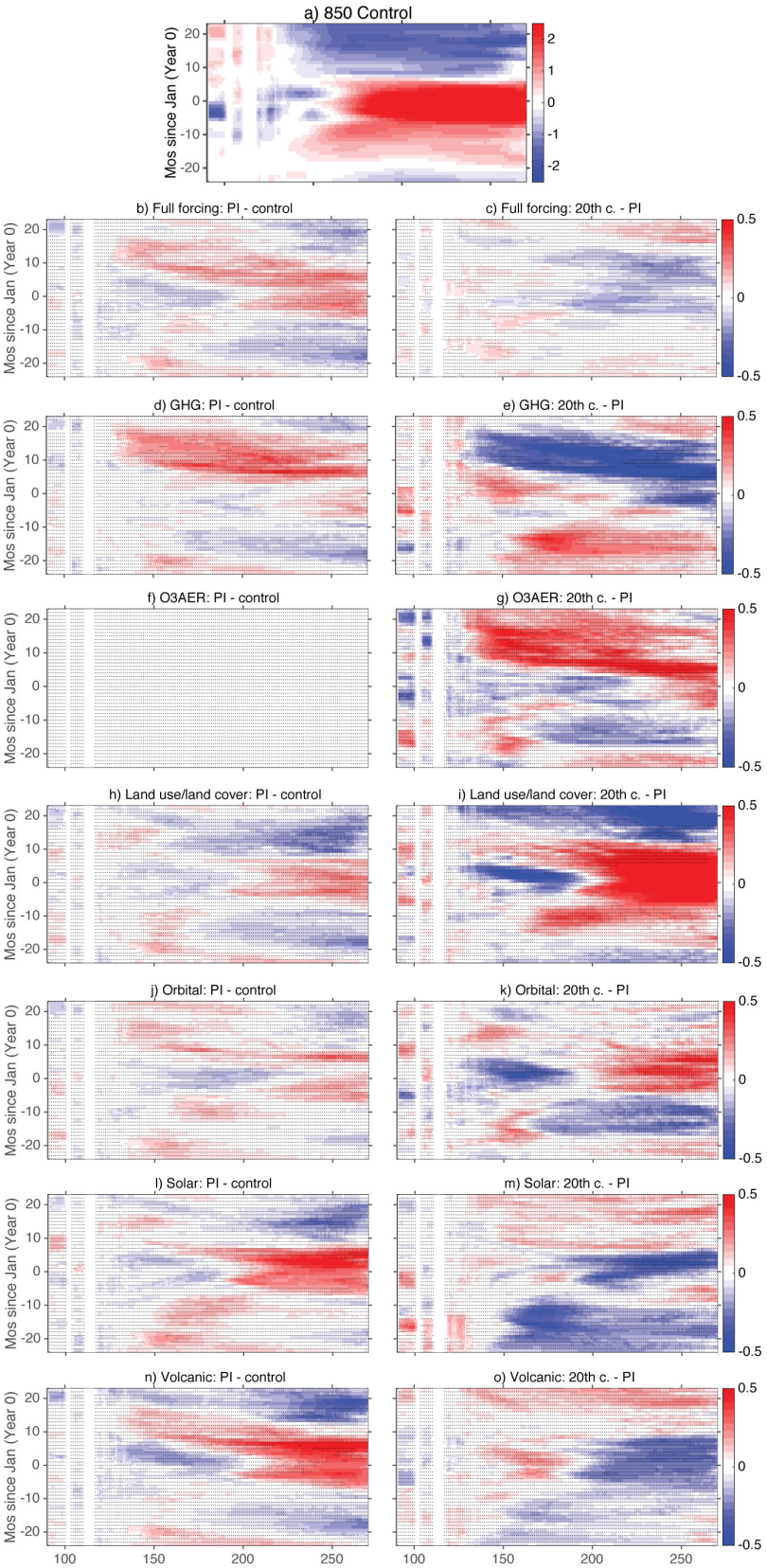

Fig. 7 Composite evolution of EP El Niño events in the LME ensembles, shown using a Hovmoeller diagram of SSTA over 2°S-2°N. Panel a) shows EP El Niños in the 850 control simulation; subsequent left-hand panels (b,d,f,h,j,l,n) show differences between the pre-industrial portions of the forced LME ensembles relative to the control, and right-hand panels (c,e,g,i,m,o) show differences between the 20th century and pre-industrial portions of individual LME ensembles. Stippling indicates that a Wilcoxon rank-sum test at that grid point resulted in SST anomalies indistinguishable from one another at 90% significance. Panel f) is blank since the 850 control is used as the pre-industrial portion of the O3AER ensemble.

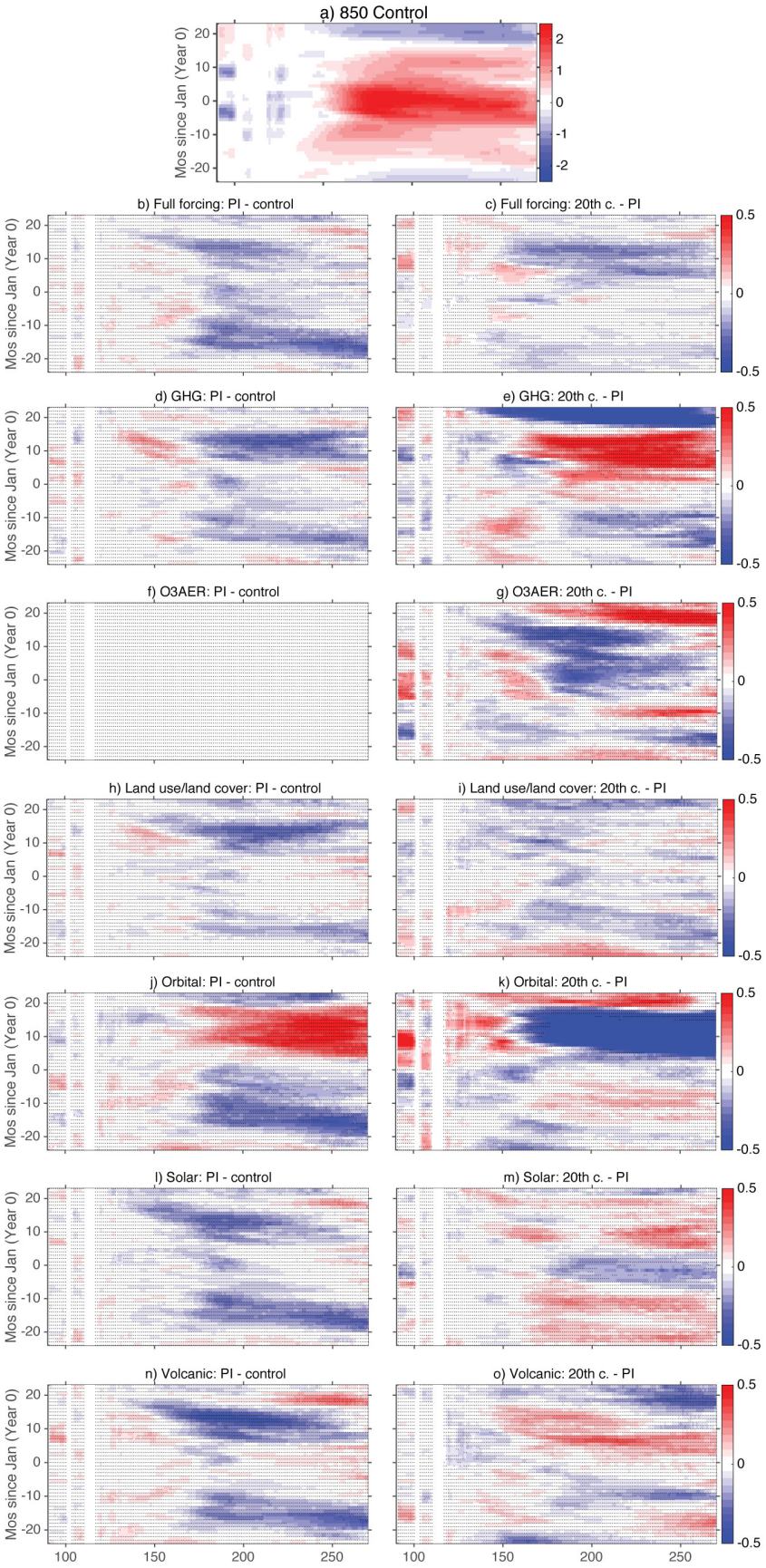

Fig. 8 Same as Figure 7, for CP El Niño events.

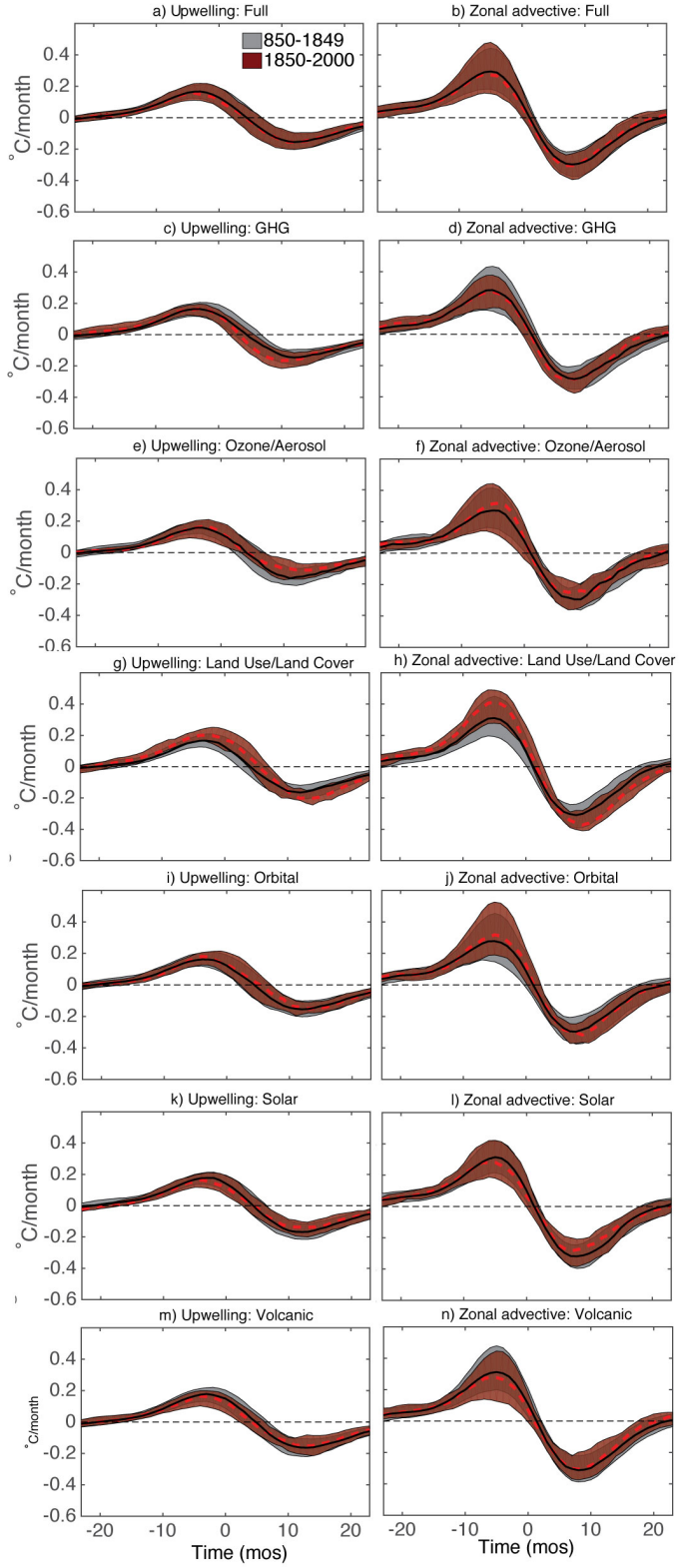

Fig. 9 Composite evolution of the upwelling feedback (left) and zonal advective feedback (right) terms in the mixed-layer heat budget for the pre-industrial (gray) and 20th century (red) portions of the LME ensembles. All budget terms have been averaged over the 'NINO3m' region (2.5°S-2.5°N, 190-250°E), and composited over Eastern Pacific El Niño events as defined by the metric of Kao and Yu (2009). Time is given in units of months since January of the year in which the El Niño peaks ('Year 0'). Envelopes indicate the interquartile range associated with feedbacks as a function of time, and the black solid and red dashed lines the medians during the pre-industrial and 20th century, respectively.

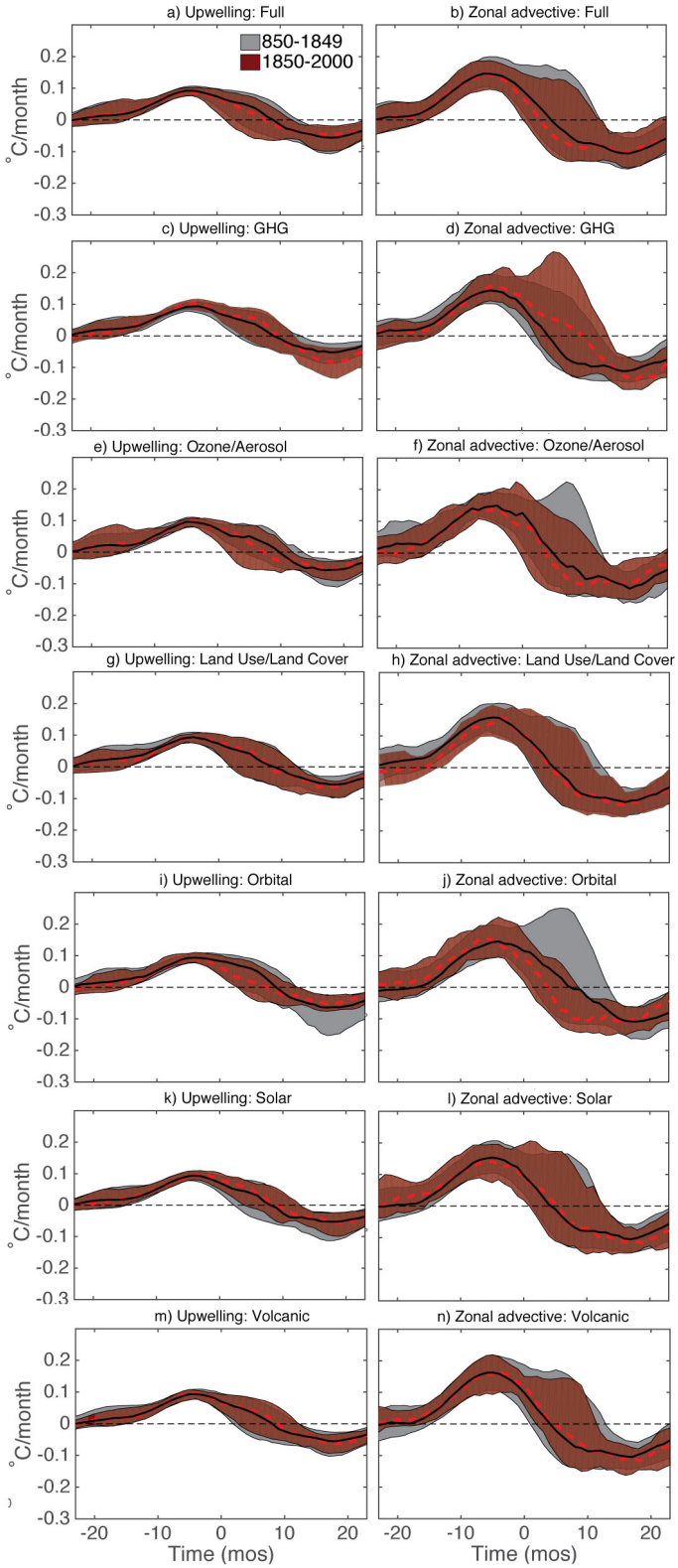

Fig. 10 Same as Figure 9, for Central Pacific El Niño events. Here budget terms have been averaged over the 'NINO4m' region (2.5°S-2.5°N, 140-190°E).

References

Ashok, K., S. Behera, A. Rao, H. Weng, and T. Yamagata, 2007: El Niño Modoki and its teleconnection,. *Journal of Geophysical Research*, **112**, C11 007, doi:10.1029/2006JC003798.

Bellenger, H., E. Guilyardi, J. Leloup, M. Lengaigne, and J. Vialard, 2014: ENSO representation in climate models: from CMIP3 to CMIP5. *Climate Dynamics*, dOI:10.1007/s00382-013-1783-z.

Berger, A., 1978: Long-term variations of daily insolation and quaternary climatic changes. *Journal of the Atmospheric Sciences*, **35**, 2362–2367.

Capotondi, A., 2013: ENSO diversity in the NCAR CCSM4 climate model. *Journal of Geophysical Research-Oceans*, **118**, 4755–4770, doi:10.1002/jgrc.20335.

Capotondi, A., and P. D. Sardeshmukh, 2015: Optimal precursors of different types of ENSO events. *Geophysical Research Letters*, **42**, 9952–9960.

Capotondi, A., and Coauthors, 2015: Understanding ENSO diversity. *Bulletin of the American Meteorological Society*, **96**, 921–938, doi: http://dx.doi.org/10.1175/BAMS-D-13-00117.1.

Cobb, K., C. D. Charles, H. Cheng, R. L. Edwards, H. R. Sayani, and N. Westphal, 2013: Highly variable El Niño-Southern Oscillation throughout the Holocene. *Science*, **339**, 67–70, doi: 10.1126/science.1228246.

Collins, M., and Coauthors, 2010: The impact of global warming on the tropical Pacific Ocean and El Niño. *Nature Geoscience*, **3**, 391–397, doi:10.1038/NGEO868.

Di Nezio, P., B. Kirtman, A. Clement, S.-K. Lee, G. Vecchi, and A. Wittenberg, 2012: Mean climate controls on the simulated response of ENSO to increasing greenhouse gases. *Journal of Climate*, **25**, 7399–7420.

Fasullo, J. T., B. L. Otto-Bliesner, and S. Stevenson, 2016: ENSO's Changing Influence on Heat Waves and Wildfire in a Changing Climate. *Nature Climate Change*, submitted.

Fedorov, A. V., and S. G. Philander, 2000: Is El Niño changing? *Science*, **288**, 1997–2002.

Gao, C. C., A. Robock, and C. Ammann, 2008: Volcanic forcing of climate over the past 1500 years: an improved ice core-based index for climate models. *Journal of Geophysical Research*, **113**, D23 111, doi: 10.1029/2008JD010239.

Graham, F. S., J. N. Brown, C. Langlais, S. J. Marsland, A. T. Wittenberg, and N. J. Holbrook, 2014: Effectiveness of the Bjerknes stability index in representing ocean dynamics. *Climate Dynamics*, **43**, 2399–2414, dOI 10.1007/s00382-014-2062-3.

Huang, B., Y. Xue, D. Zhang, A. Kumar, and M. J. McPhaden, 2010: The NCEP GODAS Ocean analysis of the Tropical Pacific mixed layer heat budget on seasonal to interannual time scales. *Journal of Climate*, **23 (18)**, 4901–4925, doi:10.1175/2010JCLI3373.1.

Hurtt, G. C., and Coauthors, 2011: Harmonization of land-use scenarios for the period 15002100: 600 years of global gridded annual land-use transitions, wood harvest, and resulting secondary lands. *Climatic Change*, **109**, 117–161, doi:10.1007/s10584-011-0153-2.

Kalnay, E., and M. Cai, 2003: Impact of urbanization and land-use change on climate. *Nature*, **423**, 528–531.

Kao, H.-Y., and J.-Y. Yu, 2009: Contrasting Eastern-Pacific and Central-Pacific Types of ENSO. *Journal of Climate*, **22**, 615–632, doi:10.1175:/2008JCLI2309.1.

Karamperidou, C., P. M. DiNezio, A. Timmermann, F.-F. Jin, and K. M. Cobb, 2015: The response of ENSO flavors to mid-Holocene climate: Implications for proxy interpretation. *Paleoceanography*, **30 (5)**, 527–547.

Kay, J. E., and Coauthors, 2015: The Community Earth System Model (CESM) Large Ensemble Project: A Community Resource for Studying Climate Change in the Presence of Internal Climate Variability. *Bulletin of the American Meteorological Society*, doi:10.1175/BAMS-D-13-00255.1.

Kessler, W., 2002: Is ENSO a cycle or a series of events? *Geophysical Research Letters*, **29 (23)**, 2125, doi:10:1029/2002GL015924.

Kug, J.-S., S.-I. An, Y.-G. Ham, and I.-S. Kang, 2010: Changes in El Niño and La Niña teleconnections over North Pacific-America in the global warming simulations. *Theor. Appl. Climatol.*, dOI 10.1007/s00704-009-0183-0.

Lamarque, J.-F., and Coauthors, 2010: Historical (18502000) gridded anthropogenic and biomass burning emissions of reactive gases and aerosols: Methodology and application. *Atmos. Chem. Phys.*, **10**, 7071–7039,

doi:10.5194/acp-10-7017-2010.

Large, W. G., G. Danabasoglu, S. C. Doney, and J. C. McWilliams, 1997: Sensitivity to Surface Forcing and Boundary Layer Mixing in a Global Ocean Model: Annual-Mean Climatology. *Journal of Physical Oceanography*, **27**, 2418–2447.

Marsh, D. R., M. J. Mills, D. E. Kinnison, J.-F. Lamarque, N. Calvo, and L. M. Polvani, 2013: Climate Change from 1850 to 2005 Simulated in CESM1(WACCM) . *Journal of Climate*, **26**, 7372–7391, doi:10.1175/JCLI -D-12-00558.1.

McGregor, S., A. Timmermann, and O. Timm, 2010: A unified proxy for ENSO and PDO variability since 1650. *Climate of the Past*, **6**, 1–17.

McPhaden, M. J., T. lee, and D. McClurg, 2011: El Nino and its relationship to changing background conditions in the tropical Pacific. *Geophysical Research Letters*, **38**, L15 709, doi:10.1029/2011GL048275.

Otto-Bliesner, B., and Coauthors, 2016: Climate Variability and Change since 850 C.E.: An Ensemble Approach with the Community Earth System Model (CESM). *Bulletin of the American Meteorological Society*, 735–754, doi:10.1175/BAMS-D-14-00233.1.

Pacanowski, R. C., and S. M. Griffies, 1999: *MOM 3.0 manual*. NOAA/Geophysical Fluid Dynamics Laboratory Rep., 680 pp.

Philip, S., and G. van Oldenborgh, 2006: Shifts in ENSO coupling processes under global warming. *Geophysical Research Letters*, **33**, L11 704.

Pielke, R. A. S., G. Marland, R. A. Betts, T. N. Chase, J. L. Eastman, J. O. Niles, D. d. S. Niyogi, and S. W. Running, 2002: The influence of land-use change and landscape dynamics on the climate system: relevance to climate-change policy beyond the radiative effect of greenhouse gases. *Philosophical Transactions of the Royal Society A*, **360**, 1705–1719, dOI: 10.1098/rsta.2002.1027.

Pongratz, J., T. Raddatz, C. H. Reick, M. Esch, and M. Claussen, 2009: Radiative forcing from anthropogenic land cover change since AD 800. *Geophysical Research Letters*, **36**, L02 709, doi:10.1029/ 2008GL036394.

Ropelewski, C. F., and M. S. Halpert, 1987: Global and regional scale precipitation patterns associated with the El Niño/Southern Oscillation. *Monthly Weather Review*, **114**, 2352–2362.

Schmidt, G. A., and Coauthors, 2011: Climate forcing reconstructions for use in PMIP simulations of the last millennium (v1.0). *Geoscientific Model Development*, **4**, 33–45.

Stevenson, S., 2012: Changes to ENSO Strength and Impacts in the CMIP5 Models. *Geophysical Research Letters*, **39**, L17 703.

Stevenson, S., B. Fox-Kemper, and M. Jochum, 2012a: Understanding the ENSO-CO_2 Link Using Stabilized Climate Simulations . *Journal of Climate*, **25**, 7917–7936, doi:http://dx.doi.org/10.1175/JCLI-D-11-00546.1.

Stevenson, S., B. Fox-Kemper, M. Jochum, R. Neale, C. Deser, and G. Meehl, 2012b: Will there be a significant change to El Niño in the 21st century? *Journal of Climate*, **25**, 2129–2145, CCSM4 special issue. doi:10.1175/JCLI-D-11-00252.1.

Stevenson, S., B. Fox-Kemper, M. Jochum, B. Rajagopalan, and S. Yeager, 2010: Model ENSO Validation Using Wavelet Probability Analysis. *Journal of Climate*, **23**, 5540–5547.

van Oldenborgh, G., S. Philip, and M. Collins, 2005: El Niño in a changing climate. *Ocean Science*, **1**, 81–95.

Vecchi, G., and B. Soden, 2007: Global Warming and the Weakening of the Tropical Circulation. *Journal of Climate*, **20**, 4316–4340, doi:10.1175/JCLI4258.1.

Vecchi, G., B. Soden, A. Wittenberg, I. Held, A. Leetmaa, and M. Harrison, 2006: Weakening of tropical Pacific atmospheric circulation due to anthropogenic forcing. *Nature*, **44**, 72–75, doi:10.1038/nature04744.

Vieira, L. E. A., S. K. Solanki, N. A. Krivova, and I. Usoskin, 2011: Evolution of the solar irradiance during the Holocene. *Astron. Astrophys.*, **531**, A6, doi:10.1051/0004-6361/201015843.

Wittenberg, A. T., 2009: Are historical records sufficient to constrain ENSO simulations? *Geophysical Research Letters*, **36**, L12 702.

Xie, S.-P., C. Deser, G. Vecchi, J. Ma, H. Teng, and A. Wittenberg, 2010: Global Warming Pattern Formation: Sea Surface Temperature and Rainfall. *Journal of Climate*, **23**, 966–986.

435 Yeh, S.-W., J.-S. Kug, B. Dewitte, M.-H. Kwon, B. P. Kirtman, and F.-F. Jin, 2009: El Niño in a changing
436 climate. *Nature*, **461**, 511–514, doi:10.1038/nature08316.
437 Yu, J.-Y., Y. Zou, S. T. Kim, and T. Lee, 2012: The changing impact of El Nino on US winter temperatures.
438 *Geophysical Research Letters*, **39**, L15 702, doi:10.1029/2012GL052483.